

**Velocity dispersion of plate acoustic waves in a multidomain phononic superlattice**

I. V. Ostrovskii, A. B. Nadtochiy,\* and V. A. Klymko

*Department of Physics and NCPA, University of Mississippi, University, Mississippi 38677, USA*

(Received 12 March 2010; revised manuscript received 21 May 2010; published 16 July 2010)

The phase and group velocities are considered for the eight lowest plate acoustic waves (PAWs) propagating in a periodically poled lithium niobate (PPLN) wafer. The PPLN turns to be a specific multidomain phononic superlattice (MPS) that has identical mechanical properties throughout the crystalline wafer but opposite-sign piezoelectric constants in the inversely poled adjacent domains. Dispersion of the velocities is calculated theoretically and verified experimentally. The group velocity tends to zero when PAW frequency approaches the stop-band limit at the first Brillouin-zone boundary. Near the stop-band cutoff frequencies, PAW modes in MPS have a strong dispersion that can be used for a number of applications.

DOI: [10.1103/PhysRevB.82.014302](https://doi.org/10.1103/PhysRevB.82.014302)

PACS number(s): 77.84.-s, 68.65.Cd, 43.20.Mv

**I. INTRODUCTION**

Interest in propagation of the acoustic waves in two-dimensional (2D) and periodic structures has grown in recent years because of the specific properties of acoustic superlattices. Existence of a “phononic” band gap was shown for a number of the periodic media of propagation and acoustic waves including 2D phononic crystal plates. Historically, a frequency-selective transmission of phonons by GaAs/Al<sub>0.5</sub>Ga<sub>0.5</sub>As superlattice was detected for the first time back in 1979,<sup>1</sup> and the “dielectric” phonon filter was proposed.<sup>1</sup> The first usage of acousto-optic interaction for observing acoustic phonons in superlattice dates back in 1987.<sup>2</sup> In that work, the phononic stop bands were optically detected in the acoustic superlattice consisting of In<sub>0.15</sub>Ga<sub>0.85</sub>As and AlAs layers. Very unusual and interesting media may possess the double properties of both photonic and phononic crystals. Such solids may also be referred to as “optomechanical crystals.”<sup>3</sup> The simultaneous handling of photons and phonons in these periodic structures may be a scientific basis for new interactions in solids, and following acousto-optic and acoustoelectronic applications. For instance, a coupling of 200 THz photons with 2 GHz phonons was achieved in a planar silicon-chip-based optomechanical crystal.<sup>3</sup> At nanometer scale, it was demonstrated as an “optomechanical cavity” in which localization of the optical and mechanical energies was achieved.<sup>4</sup> Another contemporary example, at micrometer scale, is a periodically poled ferroelectric such as LiNbO<sub>3</sub> wafer. It is known as a photonic crystal but recently it was also shown to have the acoustic stop bands in the dispersion relations  $\omega(k)$ .<sup>5</sup> In the phononic solids, it is usually considered a band structure with acoustic forbidden zones but a question of velocity dispersion within the Brillouin zone is not yet mentioned even for the acoustic phononic waveguides.<sup>6–10</sup> The frequency bands were also demonstrated for a water-based composite phononic media.<sup>11</sup> However, a velocity dispersion of PAW is important for understanding the transport and propagation phenomena for further applications. For example, the solids with acoustic phononic properties may be a kind of acoustic noise trap or effective filter absorbing vibrations of certain frequencies only and velocity dispersion is important for comprehension of PAW in the phononic superlattices. In addition, the veloci-

ties of PAW are not considered so far in a periodic structure that has identical elastic constants and densities in two members of the superlattice such as periodically poled LiNbO<sub>3</sub> (PPLN) or LiTaO<sub>3</sub>. It is not obvious at all that such elastically uniform media may have different velocity dispersion for acoustic modes in comparison to a single ferroelectric crystal without domain inversion. Since this type of periodic ferroelectric solids is widely investigated with regard to the nonlinear optical, acousto-optical, and acoustoelectronic phenomena, the dispersions of phase and group velocities of allowed PAW modes are of fundamental scientific interest. Generally speaking, the stop bands may be guessed based on an effective interaction between ultrasound and ferroelectric domains. The interactions were demonstrated on different phenomena such as acoustical memory,<sup>12,13</sup> acoustoelectric transduction,<sup>14–16</sup> and domain resonance.<sup>17</sup> The reality of stop bands in PPLN wafer was independently proved by observing a strong decrease in group velocities of three PAW modes near the stop-band frequencies.<sup>5</sup> However, the velocity dispersion of PAW within the Brillouin zone remains unknown. Note: ever since the first publications on acoustic waves<sup>18–23</sup> and optoacoustic excitations<sup>24,25</sup> in bulk ferroelectric multidomain phononic superlattice (MPS), the question of ultrasound velocity dispersion was not a concern. However, the contemporary wide range of PPLN-wafer applications raises the question on the dispersions of phase and group velocities of PAW modes in these acoustic waveguides.

The present work investigates the dispersion of phase and group velocities of eight PAW modes propagating along the  $x$  axis in the  $z$ -cut PPLN wafer. To some extent, this research was inspired by the existence of stop bands in acoustic dispersion  $\omega(k)$  for PAW in ZX-cut PPLN (ZX-PPLN). The eight lowest PAW modes are analyzed theoretically and experimentally in a frequency range from 0 to 10 MHz.

**II. COMPUTATION OF PHASE AND GROUP-VELOCITY DISPERSION**

The velocities are calculated and measured as shown in Fig. 1. The coordinate system is fixed to the plate with the  $z$  axis normal to the plate surface and the  $x$  axis in the direction of the stage motion. The phase and group velocities may be

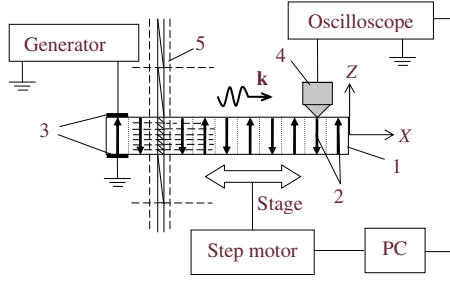


FIG. 1. (Color online) The ZX-cut PPLN wafer and experimental setup for excitation and detection of PAW propagating along the  $x$  axis. 1—PPLN plate, 2—domains with periodically inverted polarization, 3—metal electrodes for PAW excitation, 4—piezoelectric micropick-up output transducer, and 5—mesh for FEM computation.

calculated from the dispersion laws  $\omega(k)$  of the corresponding acoustic modes. The dispersion relations  $\omega(k)$ , in turn, are obtained by using 2D numerical model based on the finite-element method (FEM). In this model, the domains with inverse polarization are taken into account by inverting the sign of piezoelectric constants  $e_{m,ij}$ . This reflects the fact that the same mechanical strain applied to a periodically poled MPS generates opposite piezoelectric fields in the domains with inverse polarization. If a single-crystal lithium niobate (SCLN) wafer is computed, then the piezoelectric constants  $e_{m,ij}$  do not change their sign with  $x$  variable. In the FEM model for PPLN and SCLN, the plate is assumed to be infinite in the  $y$  direction. The model was first validated by calculating the PAW dispersion curves for the SCLN wafer by two methods including the FEM computation and established method of partial waves. The results obtained by the both methods were identical. In Fig. 1 is shown a linear nonuniform triangular mesh representing the crystalline plate and air above and below this plate. The accuracy of the FEM model mostly depends on the mesh density; a denser mesh results in a more accurate solution. A typical mesh used in our calculations consists of  $1501 \times 21$  points and covers the cross section of  $75 \times 0.5$  mm<sup>2</sup>. The electric field outside the piezoelectric plate is included in the model by extending the numerical mesh in the air outside the plate, as shown in Fig. 1.

The solution of this problem is based on the Hamilton's variational principle extended to the piezoelectric wafer of unit width along the  $y$  axis. For this case, the first-order variation in the Lagrangian is equalized to zero by Eq. (1),

$$\delta \int (W_{kin} - W_{st} + W_{d,C} + W) dt = 0. \quad (1)$$

The components of PAW total energy are kinetic energy of vibrating plate  $W_{kin}$ , elastic energy of crystal deformation in an acoustic field  $W_{st}$ , and energy of piezoelectric field inside crystal  $W_{d,C}$ . They are calculated by Eq. (2) below,

$$W_{kin} = \frac{1}{2} \int \rho \cdot \dot{u}^2 dx dz; \quad W_{st} = \frac{1}{2} \int \mathbf{S}^t \cdot \mathbf{T} dx dz;$$

$$W_{d,C} = \frac{1}{2} \int \mathbf{D} \cdot \mathbf{E} dx dz, \quad (2)$$

where  $\rho$  is the density,  $u$  is the acoustic displacement,  $E_i = -\frac{\partial \varphi}{\partial x_i}$ , and  $\mathbf{D}_i$  are the components of electric field and displacement, respectively;  $\varphi$  is the electric potential; the terms  $\mathbf{S}^t$  and  $\mathbf{T}$  represent tensors of acoustic strain and stress, respectively. In addition to the PAW modes, an external force exciting the waves must be taken into account. The external force  $\mathbf{F}$  applied at the location of the input transducer creates an acoustic displacement  $\mathbf{u}$ , and therefore the energy  $W$  brought into the wafer by this force may be computed by Eq. (3),

$$W = \int \mathbf{u} \cdot \mathbf{F} dx_3. \quad (3)$$

The results of FEM computation are identical for two methods of PAW excitation with the mechanical force or electric voltage, as shown in Fig. 1. To compute the functional of Eq. (1), it is necessary to know all variables in Eqs. (2) and (3), which in turn, may be calculated by using the standard equations of motion and electrodynamics for piezoelectric medium. In addition to these equations, the standard boundary conditions are applied: (a) zero acoustic stress at free plate surfaces and (b) continuity of normal electric displacement at crystal-air interfaces.

The variational Eq. (1), along with the Eqs. (2) and (3) and the appropriate boundary conditions, is solved numerically. The FEM calculations return four arrays that contain the components of acoustical displacement  $U_m(x_i, \omega_j)$ ,  $m = 1 \dots 3$ , and the electric potential  $\varphi \equiv U_4(x_i, \omega_j)$  at the discrete points  $x_i$  at the frequencies  $\omega_j$ . The discrete Fourier transform is applied to these arrays to calculate their Fourier images in  $\omega-k$  domain:  $U_m^F(k_i, \omega_j)$ ,  $m = 1, \dots, 4$ ;  $k = 2\pi/\lambda$ . The total Fourier image amplitude is further calculated by the Eq. (4) below,

$$U^F(k_i, \omega_j) = \sqrt{\sum_{m=1}^4 [U_m^F(k_i, \omega_j)]^2}. \quad (4)$$

The peaks values of  $U^F(k, \omega)$  or  $U^F(\omega, k)$  form the FEM dispersion relations for the PAW. In this way, the dispersion relations  $\omega(k)$  of PAW modes are represented by the matrix of Fourier image  $U^F(\omega, k)$ , which is actually a set of points in  $\omega-k$  domain. These matrices were calculated for both the SCLN plate and PPLN wafer with 300- $\mu$ -wide domains, which are further used in the experiments. Note: the resultant dispersion laws  $\omega(k)$  are the same if any of the amplitudes  $U_m^F(k_i, \omega_j)$  are used to find the  $\omega(k)$ . However, those dispersion relations calculated by Eq. (4) have the smallest uncertainty.

The micropicture of a central part of the experimental PPLN wafer is given in Fig. 2. The dispersion curves themselves for ZX-cut SCLN (ZX-SCLN) may be found in Ref. 26 and for ZX-PPLN in Ref. 5. The last step is to find the dispersions of phase  $V_p(\omega)$  and group  $V_g(\omega)$  velocities. They are calculated as  $V_p(\omega) = \omega(k)/k$  and  $V_g = d\omega(k)/dk$ , respectively. Note: one can calculate the group velocity  $V_g$  as the

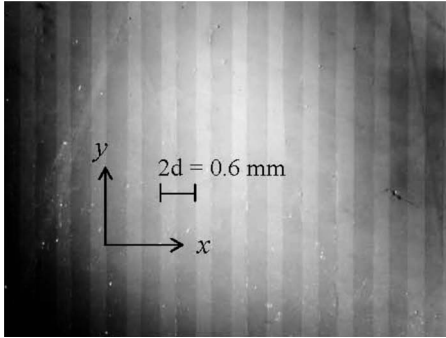


FIG. 2. Micropicture of the PPLN sample LN-MD-1 taken through a polarizing microscope. The darker strips are domains with inverted polarization and the light gray strips are domains with original polarization. The width of two adjacent domains is 0.6 mm along the crystallographic  $x$  axis.

derivative  $d\omega(\mathbf{k})/d\mathbf{k}$  because  $V_g$  is parallel to the wave vector  $\mathbf{k}$  in the particular case of PAW propagating along the  $x$  axis in the  $z$ -cut  $\text{LiNbO}_3$  wafer.<sup>27</sup> The final theoretical results are presented by solid lines in Figs. 3 and 4 for the phase velocity, and in Fig. 5 for the group velocity. The PAW modes in  $3m$ -symmetry solids have all three orthogonal components of the acoustical displacement. However, some modes have dominant shear horizontal (SH) displacement  $U_y$ , and can be called quasishear waves. The other type of PAW modes has dominant  $U_x$  and  $U_z$  displacements, and can be called quasi-Lamb waves. In Figs. 3–5, the modes  $SS_0$ ,  $SA_1$ , and  $SS_1$  are quasishear waves, sometimes called SH modes. All other modes including  $A_0$ ,  $S_0$ ,  $A_1$ ,  $S_1$ , and  $S_2$  are quasi-Lamb waves.

Both families of the plate waves fall into two groups, namely, symmetrical (S) and antisymmetrical (A); they correspondingly have symmetrical or antisymmetrical distribu-

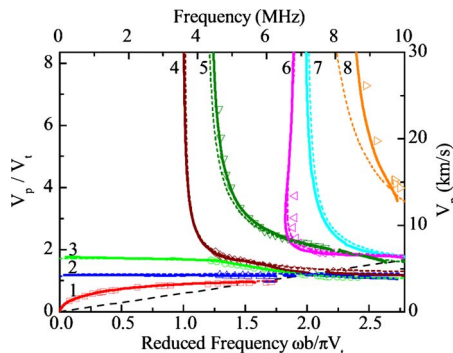


FIG. 3. (Color online) Dispersion of phase velocity for eight PAW modes in  $\text{LiNbO}_3$  wafer. The solid and dotted lines are FEM computations for multidomain PPLN and single-crystal SCLN wafer, respectively, plate thickness is 0.5 mm. The points are experimental data taken from the PPLN sample LN-MD-1 with 0.3 mm domains as shown in Fig. 2. The modes are numbered as follow: 1— $A_0$ , 2— $SS_0$ , 3— $S_0$ , 4— $SA_1$ , 5— $A_1$ , 6— $S_1$ , 7— $SS_1$ , and 8— $S_2$ . The stop bands occur along the inclined dashed line that corresponds to the boundary of first Brillouin zone in the multidomain phononic superlattice at  $k=\pi/d$ . The first Brillouin zone is above dashed line and the second Brillouin zone is below this line.  $V_t=3.59$  km/s.

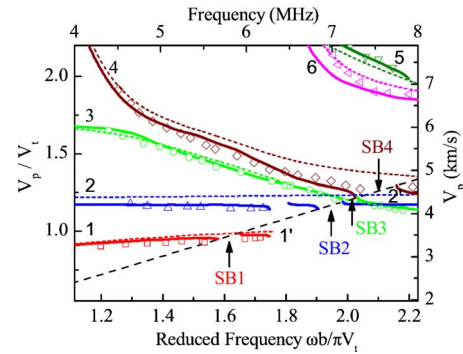


FIG. 4. (Color online) Dispersion of phase velocity for six low-order PAW modes in  $\text{LiNbO}_3$  wafer near boundary of the first Brillouin zone in PPLN. The inclined dashed line corresponds to  $k=\pi/d$ . The first Brillouin zone is above and the second is below the dashed line. The solid and dotted lines are FEM computations for PPLN and SCLN 0.5-mm-thick wafer, respectively. The points are experimental data taken from the multidomain sample LN-MD-1 with domain period  $d=0.3$  mm. The plots are: 1— $A_0$ , 2— $SS_0$ , 3— $S_0$ , 4— $SA_1$ , 5— $A_1$ , and 6— $S_1$ . In the second Brillouin zone, as an example, the modes 1 and 2 are marked as 1' and 2', respectively. The stop bands are indicated by SB1 through SB4 for the four lowest modes.  $V_t=3.59$  km/s.

tion of the acoustical displacements with respect to the neutral or central plane  $z=0$  running between two surfaces of the wafer, Fig. 1.

### III. EXPERIMENTAL DETAILS

The dispersion properties of phase and group velocities can be verified by using experimentally measured frequencies  $\omega_{exp}$  and wave vectors  $k_{exp}$  for observed PAW modes. The experimental setup for excitation and detection of PAW in a PPLN wafer is shown in Fig. 1. The sample is placed on a computerized moving stage. The initial wafer is 3 in. in diameter, 0.5-mm-thick optical grade plate with both surfaces polished. The accuracy of crystallographic cut is better than  $5'$  for the  $z$  axis, and  $10''$  for the  $x$  and  $y$  axes. The polarization inversion was obtained by applying the 22 kV/mm electric field in the  $z$  direction. The resultant multidomain array consists of a sequence of 0.3-mm-wide inversely poled domains, as shown in Fig. 2. The acoustic waves are excited by applying a broadband rf voltage to the input metal electrodes, which are extended in the  $y$  direction. The experimental output signal at plate surface is an acoustic displacement  $U_{exp}(x_f, t_g)$ . It is detected by the piezoelectric microtransducer brought into contact with the wafer in a narrow spot of 0.15 mm, which is smaller than domain width. The pick-up is mostly sensitive to a vertical component of total displacement. However, the other components may be detected because of the Poisson effect. During experiments, the stage is set in motion by a computer-controlled step motor. In every single run, the stage makes 800 steps to cover the sample length. The output transducer, 4 in Fig. 1, reads the wave forms of propagating PAW on the plate surface at the initial location of the transducer plus at every of 800 successive stops. The electric signal from the output trans-

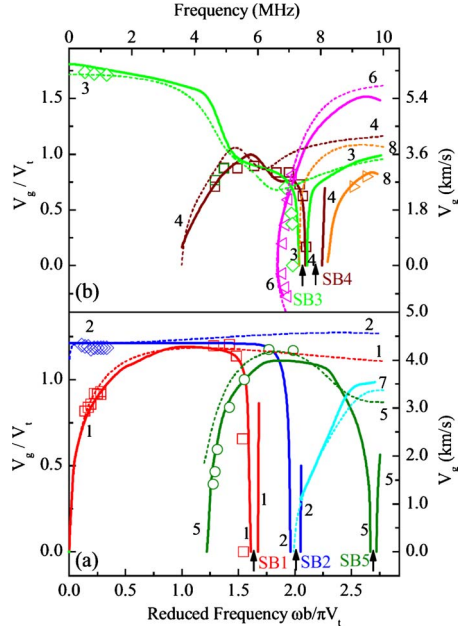


FIG. 5. (Color online) Dispersion of group velocity for eight PAW modes in LiNbO<sub>3</sub> wafer. The solid and dotted lines are FEM computations for PPLN and SCLN 0.5-mm-thick wafers, respectively. The points represent experimental data taken from the PPLN sample LN-MD-1,  $d=0.3$  mm. In panels (a) and (b), the plots are: 1— $A_0$ , 2— $SS_0$ , 3— $S_0$ , 4— $SA_1$ , 5— $A_1$ , 6— $S_1$ , 7— $SS_1$ , and 8— $S_2$ . The modes numbered 1–5 in PPLN clearly have the stop bands that are shown by SB notations with mode's number. The PAW modes in SCLN, dotted plots, do not have stop bands.  $V_t=3.59$  km/s.

ducer is amplified and sent to the digital oscilloscope LeCroy 9400, where it is digitized and then stored in a computer. During each single stop at 801 locations  $x_f$  ( $f=1, 2, \dots, F=801$ ), the measurements are taken 2000 times at successive instants  $t_g$  ( $g=1, 2, \dots, G=2000$ ). Thus, the experimental data are taken in the form of a matrix ( $F \times G=801 \times 2000$ ), which is filled with the measured discrete values of 2000 times detected wavelet amplitude at times  $t_g$  during each stop of 801  $x_f$  locations along sample length. After that, a digital double Fourier transform is applied to the matrices of experimentally measured acoustical displacement  $U_{exp}(x_f, t_g)$ . The resultant matrix of the Fourier image  $U_{exp}^F(\omega_g, k_f)$  gives the experimental dispersion relations  $\omega_{exp}(k_{exp})$  of detected waves in matrix form. The examples of experimental dispersion curves for single-crystal sample ZX-SCLN-1 is presented in Ref. 25 and for multidomain specimen ZX-PPLN-MD-1 in Ref. 5. The last step is obtaining experimental points for the phase ( $V_{p,exp}$ ) and group ( $V_{g,exp}$ ) velocities as  $V_{p,exp}(\omega)=\omega_{exp}(k_{exp})/k_{exp}$  and  $V_{g,exp}(\omega)=d\omega_{exp}(k_{exp})/dk_{exp}$ . Experimental results are presented by the points in Figs. 3 and 4 for the phase velocities, and Figs. 5(a) and 5(b) for the group velocities. Note that not all of the PAW modes are experimentally detected in the frequency range used for the theoretical computations, from 0 to 10 MHz. The point is a PAW mode must be first excited in order to be detected. Since different waves have complicated dependencies of their electromechanical coupling coefficients versus frequency,<sup>26</sup> the PAW modes are excited only in certain fre-

quency ranges, where their electromechanical coupling coefficient is large enough to convert input rf voltage into detectable acoustic displacement.

#### IV. DISCUSSION

In all Figs. 3–5, the solid lines and experimental points are plotted for the multidomain sample ZX-PPLN-MD-1, and the dotted lines are plotted for the single-crystal sample ZX-SCLN-1. The PAW velocities are normalized to the velocity of a transverse-acoustic wave ( $V_t=3.59$  km/s) propagating along the  $z$  axis in a bulk LiNbO<sub>3</sub> crystal. The velocities are plotted as a function of dimensionless reduced frequency  $\Omega=\omega b/\pi V_t$ , where  $b$  is plate thickness. This reference frame allows usage of the results obtained for the wafers of arbitrary thickness and waves of different frequency than we used in this work. Inside the first Brillouin zone, the FEM computations for multidomain and single-crystal plates return close phase velocities for the modes numbered 1, 2, 3, 4, and 6, Figs. 3 and 4. However, near the first Brillouin-zone boundary (BZB), which is shown by the dashed lines in Figs. 3 and 4, there are significant differences in the modes dispersion. In Fig. 5, the numerical curves for PAW in MPS are basically in a good agreement with the experimental points taken from the PPLN sample.

The three zero-order modes, plots number 1, 2, and 3 in the figures, do exist when frequency tends to zero. The zero antisymmetrical quasi-Lamb mode  $A_0$ , plot 1 in the figures, is highly dispersive at  $\Omega < 0.5$ . Its phase velocity increases with frequency and approaches the velocity of the transverse-acoustic wave in a bulk LiNbO<sub>3</sub> crystal. However, when frequency is increasing, the mode 1 is the first to reach BZB shown by dashed line in Figs. 3 and 4. At the BZB, when  $k=\pi/d$ , the mode 1 has a discontinuity in phase velocity denoted as SB1 in Fig. 4, it is a stop band of this mode. The zero quasishear symmetrical mode  $SS_0$ , number 2 in the figures, is low dispersive, and its phase velocity is nearly constant. In proximity of BZB, mode 2 has its stop band denoted as SB2 in Fig. 4. In Fig. 5, the PAW modes including  $SS_0$  and  $S_0$  (plots 2 and 3, respectively) are intentionally presented in two panels of Figs. 5(a) and 5(b), to show more clearly the positions of all calculated stop bands. The mode  $SS_0$ , plot 2 in Fig. 5(a), also has nearly constant group velocity up to  $f=6.3$  MHz but at frequency range  $\sim 6.8$ – $7.1$  MHz, the stop band interrupts the dispersion curve of  $SS_0$  mode. Its group velocity decreases to zero at  $\sim 6.8$  MHz. The zero symmetrical quasi-Lamb mode  $S_0$ , plot 3 in the figures, is very dispersive in the range of  $\Omega > 1.20$ , where its velocity decreases. Its stop band is marked as SB3 in Figs. 4 and 5. The higher-order modes can propagate at frequencies above 3.6 MHz, plots 4–8. The phase velocities of higher-order modes are gradually increasing with approaching their cutoff frequencies. For instance, the  $V_p$  of  $SA_1$  mode (plot 4 in Fig. 3) is rapidly rising when  $\Omega$  is changing from 1.2 down to the cutoff at  $\Omega=1$ . The dispersion curve of the  $S_1$  mode, plot 6, consists of two branches. The upper branch at  $(V_p/V_t) > 2.8$  represents the wave with opposite phase and group velocities since  $V_g=(d\omega/dk) < 0$  while the lower branch at  $(V_p/V_t) < 2.8$  represents a regular

TABLE I. The lower ( $F_L$ ) and upper ( $F_U$ ) cutoff frequencies from the experimental velocities dispersions and from the FEM computations of corresponding dispersion laws  $\omega(k)$ .

Mode	Experiment: $V_{p,\text{exp}}(\omega)^1$ ; $V_{g,\text{exp}}(\omega)^2$		Theory: $\omega(k)$	
	$F_L$ (MHz)	$F_U$ (MHz)	$F_L$ (MHz)	$F_U$ (MHz)
1 ( $A_0$ )	5.51 <sup>1</sup>	5.98 <sup>1</sup>	5.67	5.99
2 ( $SS_0$ )	6.20 <sup>1</sup>	n/a	6.84	7.12
3 ( $S_0$ )	7.13 <sup>1,2</sup>	7.49 <sup>1,2</sup>	7.23	7.43
4 ( $SA_1$ )	7.44 <sup>1</sup> , 7.33 <sup>2</sup>	7.93 <sup>1</sup> , 7.94 <sup>2</sup>	7.30	7.90
5 ( $A_1$ )	n/a	n/a	9.56	9.78

wave with positive phase and group velocities. This situation is clearly presented in Fig. 5(b), where plot 6 has a region with experimentally measured group speed below the level  $V_g=0$ . Practically it means that the directions of phase and group velocities are antiparallel.

The theory and experiment show that the PAW modes in MPS can effectively interact with the domain vibrations when mode's wavelength is equal to a double domain width,  $2d=0.6$  mm, in the wafers under study. One of the results of this interaction is existence of the stop bands that clearly appeared in Figs. 3–5 for those acoustical modes that reach BZB in the plots  $V_p(\Omega)$ . These are modes number 1–5, and the last three modes, presented by plots 6, 7, and 8, do not get to BZB at frequency  $\leq 10$  MHz. In proximity of their stop bands, the waves in MPS may have lower amplitude, and are barely detected despite stronger amplitude at lower frequencies. For instance, nondispersive mode  $SS_0$  in PPLN, solid-line plot 2 in the figures, has theoretical stop band from  $\Omega \sim 1.9$  to  $\Omega \sim 2.0$  but in the experiment the lower limit of its observation is  $\Omega=1.76$ , Fig. 4, while its upper limit is not detected at all. At the edges of stop bands, the numerical and experimental phase velocity dispersion curves are distorted, and agreement between the theory and experiment is not excellent. It can be explained by a strong reflection of PAW modes within their stop bands. However, the cutoff frequencies of the stop bands may be measured from the velocity dispersion. They are given in Table I along with the corresponding frequencies of theoretically calculated stop bands from the acoustic dispersion laws  $\omega(k)$ .

The comments on Table I: (A) for mode number 2, the disagreement of 0.64 MHz between the experimental and theoretical values of  $F_L$  may be explained by low-amplitude acoustic signal which may be detected from this wave since it has mainly a shear displacement  $U_Y$ . Because of this reason, the  $F_U$  cutoff was not experimentally detected as well. (B) The mode number 5 has a very low electromechanical coupling coefficient.<sup>26</sup> It is only less than 0.1% within reduced frequencies of  $2.3 < \Omega < 2.8$ ; the mode 5 stop band is at  $2.66 < \Omega < 2.72$ , plot 5 in Fig. 5(a). That is why this mode 5 is not detected near its stop-band frequencies  $F_L$  and  $F_U$  because the piezoelectric excitation is used in the experiment as shown in Fig. 1.

The stop bands are possible only in a multidomain waveguide such as PPLN, they do not appear in a regular single-

crystal wafer. For instance, in Figs. 3 and 4, the curves 1, 2, 3, 4, and 5 have discontinuities at acoustic wavelength  $\lambda=2d$  only for PPLN. In contrast, for the case of a single-crystal wafer, the dotted dispersion curves do not have any discontinuities. In the Figs. 5(a) and 5(b), the stop bands denoted as SB1–SB5 do exist also only for PPLN wafer. Within the stop bands, corresponding modes cannot propagate having the zero group velocities. In contrast, for a single-crystal waveguide, dotted plots in figures, the stop bands do not exist, as it is expected from the general theory of PAW (Refs. 28–31) and investigations of PAW in single-crystal wafers of  $\text{LiNbO}_3$ .<sup>26,27,32–34</sup>

## V. CONCLUSIONS

(1) The stop-band properties are revealed in the dispersion of phase and group velocities of PAW modes propagating in a two-dimensional periodically poled ferroelectric waveguide, which turns to be a specific multidomain phononic superlattice. This type of a phononic superlattice may be created by a periodical polarization inversion in the ferroelectric crystals such as lithium niobate, lithium tantalite, and other ferroelectric solids. The physical origin of stop bands is a Bragg-type reflection of the acoustic modes from the multidomain superlattice at the boundary of acoustic first Brillouin zone. It happens when a particular PAW mode has a wave vector  $k=\pi/d$ , where  $d$  is a period of the multidomain structure. In other words, the stop band occurs because a PAW mode is “trapped” within the multidomain phononic superlattice and then reflected by this superlattice when an acoustic wavelength is exactly equal to doubled superlattice period,  $\lambda=2d$ .

(2) The effect of the stop band is theoretically calculated and experimentally confirmed for the five lowest acoustic modes propagating in the  $z$ -cut PPLN wafer at reduced frequencies  $\Omega$  below 3.0, the other modes numbered 6, 7, and 8 may have their stop bands at  $\Omega > 3.0$ . This type of ferroelectric wafer is widely used for acousto-optic and nonlinear optic applications including second-harmonic generation of laser radiation. Knowing frequencies of the acoustic stop bands may be of help for developing more reliable high-intensity optical applications because an intensive laser pulse with a certain repetition rate may cause a strong mechanical stress in the multidomain superlattice due to piezoelectric and piroelectric properties of  $\text{LiNbO}_3$ . Then any resonance energy absorption associated with the stop-band frequencies or their subharmonics is not desirable.

(3) The two-dimensional finite-element model is used to calculate the dispersion curves of phase and group velocity of PAW modes in a periodically poled ZX-cut lithium niobate wafer. The dispersion of phase and group velocities of three zero modes and five higher-order modes are computed in a frequency range from 0 to 10 MHz, which corresponds to the dimensionless frequency  $\Omega=(\omega b/\pi V_l) < 3.0$ . The obtained dispersion curves presented by the solid lines in Figs. 3–5 can be used for finding phase and group velocities in the two-dimensional piezoelectric superlattices of other multidomain structures of  $C_{3V}$  symmetry. It includes different wafer thickness, other domain dimension, and another material

with different velocity  $V_t$  of bulk shear acoustic wave. The numerical results are in good agreement with the experimental data taken from the  $z$ -cut PPLN wafer.

(4) The results of this work can be used for developing different solid-state acoustoelectronic filters and other signal-processing devices. The dispersion characteristics of five PAW modes enumerated 1, 2, 3, 4, and 5 in Figs. 3 and 5 suggest the possibility of developing new ferroelectric devices such as a stop-band filter that cuts out only certain frequencies falling within the stop-band range. The high dispersion of a group velocity of PAW modes at the edges of their stop-band frequency ranges may be used for developing highly compact dispersive delay line with, respectively, high time delay. The first five modes in Figs. 3 and 5 are good candidates for this application. Note, the plate waves in SCLN do not have this particular high dispersion property because of absence of the stop bands.

(5) The comparison of the dispersion curves in Fig. 3 for PAW modes in PPLN with the same curves for PAW modes in SCLN reveals the changes in the dispersion curves due to multidomain superlattice effect. Besides nonexistent stop bands in SCLN, the PAW modes  $A_1$  and  $S_2$  (plots 5 and 8 in Fig. 3) have the cutoff frequencies higher in PPLN plate. For instance, in a single-crystal plate, the  $A_1$ -mode cutoff is at reduced frequency  $\Omega(A_1)=1$ , and the  $S_2$ -mode cutoff is at  $\Omega(S_2)=2.01$ , when  $V_p$  tends to infinity. In contrast, the corresponding cutoff frequencies in a periodically poled wafer are shifted to  $\Omega(A_1)=1.2$  and  $\Omega(S_2)=2.3$ , when  $V_p$  tends to

infinity. These changes may be explained by acoustic displacement peculiarities. Near the cutoff frequencies, the acoustical displacement in the modes  $A_1$  and  $S_2$  is primarily longitudinal along the  $x$  axis, and so the displacement is normal to the interdomain walls. Because the wave vectors tends to zero at cutoff frequencies, the corresponding wavelength is much longer than the domain size, and therefore the direction of acoustical displacement in the adjacent domains must be the same. The latter conclusion is in contradiction with the opposite piezoelectric fields inside the adjacent domains with inverse polarization. It looks like this inconsistency leads to a cancellation of the longitudinal-acoustic displacements in the multidomain array if a wavelength is much longer than domain period. This situation in turn causes a high-frequency shift in dispersion curves of the modes with mainly longitudinal displacements, plots 5 and 8 in Fig. 3. In fact, the quasi-Lamb waves  $A_1$  and  $S_2$  are canceled in PPLN near their cutoffs due to the opposite piezoelectric fields in the adjacent domains, and they resume at higher frequencies in comparison to the case of single-crystal wafer.

#### ACKNOWLEDGMENTS

This research in part was supported by the research grant FRP-2008/9, UM, and Graduate School Summer Research grant, UM. We are thankful to Mack Breazeale and Michael McPherson for useful discussions.

\*On leave from the Taras Shevchenko National University of Kyiv, Kyiv, Ukraine.

<sup>1</sup>V. Narayanamurti, H. L. Störmer, M. A. Chin, A. C. Gossard, and W. Wiegmann, *Phys. Rev. Lett.* **43**, 2012 (1979).

<sup>2</sup>D. C. Hurley, S. Tamura, J. P. Wolfe, and H. Morkoç, *Phys. Rev. Lett.* **58**, 2446 (1987).

<sup>3</sup>M. Eichenfield, J. Chan, R. M. Camacho, K. J. Vahala, and O. Painter, *Nature (London)* **462**, 78 (2009).

<sup>4</sup>M. Eichenfield, R. Camacho, J. Chan, K. J. Vahala, and O. Painter, *Nature (London)* **459**, 550 (2009).

<sup>5</sup>I. V. Ostrovskii, V. A. Klymko, and A. B. Nadtochiy, *JASA Express Lett.* **125**, EL129 (2009).

<sup>6</sup>J.-J. Chen, K.-W. Zhang, J. Gao, and J.-C. Cheng, *Phys. Rev. B* **73**, 094307 (2006).

<sup>7</sup>J. O. Vasseur, P. A. Deymier, B. Djafari-Rouhani, Y. Pennec, and A.-C. Hladky-Hennion, *Phys. Rev. B* **77**, 085415 (2008).

<sup>8</sup>M. Wilm, A. Khelif, S. Ballandras, and V. Laude, *Phys. Rev. E* **67**, 065602(R) (2003).

<sup>9</sup>T. Brunet, J. Vasseur, B. Bonello, B. Djafari-Rouhani, and A.-C. Hladky-Hennion, *J. Appl. Phys.* **104**, 043506 (2008).

<sup>10</sup>A. Khelif, B. Aoubiza, S. Mohammadi, A. Adibi, and V. Laude, *Phys. Rev. E* **74**, 046610 (2006).

<sup>11</sup>H. Sanchis-Alepuz, Y. A. Kosevich, and J. Sanchez-Dehesa, *Phys. Rev. Lett.* **98**, 134301 (2007).

<sup>12</sup>M. S. McPherson, I. Ostrovskii, and M. A. Breazeale, *Phys. Rev. Lett.* **89**, 115506 (2002).

<sup>13</sup>D. Zhou, X. Liu, and X. Gong, *Phys. Rev. E* **78**, 016602 (2008).

<sup>14</sup>E. Courjon, N. Courjal, W. Daniau, G. Lengaigne, L. Gauthier-Manuel, S. Ballandras, and J. Hauden, *J. Appl. Phys.* **102**, 114107 (2007).

<sup>15</sup>D. Yudistira, S. Benchabane, D. Janner, and V. Pruneri, *Appl. Phys. Lett.* **95**, 052901 (2009).

<sup>16</sup>I. V. Ostrovskii and A. B. Nadtochiy, *J. Appl. Phys.* **103**, 104107 (2008).

<sup>17</sup>I. V. Ostrovskii and A. B. Nadtochiy, *Appl. Phys. Lett.* **86**, 222902 (2005).

<sup>18</sup>S. W. Meeks and B. A. Auld, *Appl. Phys. Lett.* **47**, 102 (1985).

<sup>19</sup>Y.-Y. Zhu, N.-B. Ming, W.-H. Jiang, and Y.-A. Shui, *Appl. Phys. Lett.* **53**, 1381 (1988).

<sup>20</sup>Y.-Y. Zhu, N.-B. Ming, W.-H. Jiang, and Y.-A. Shui, *Appl. Phys. Lett.* **53**, 2278 (1988).

<sup>21</sup>V. I. Alshits, A. N. Darinskii, A. L. Shuvalov, V. V. Antipov, S. I. Chizhikov, and N. G. Sorokin, *Ferroelectrics* **96**, 91 (1989).

<sup>22</sup>L. Xingjiao, L. Yibing, L. Shaoping, L. E. Cross, and R. E. Newnham, *J. Phys.: Condens. Matter* **2**, 9577 (1990).

<sup>23</sup>A. L. Shuvalov and A. S. Gorkunova, *Phys. Rev. B* **59**, 9070 (1999).

<sup>24</sup>Y.-Q. Lu, Y.-Y. Zhu, Y.-F. Chen, S.-N. Zhu, N.-B. Ming, and Y.-J. Feng, *Science* **284**, 1822 (1999).

<sup>25</sup>Y.-Q. Lu, Q. Wang, Y.-X. Xi, Z.-L. Wan, X.-J. Zhang, and N.-B. Ming, *Ferroelectrics* **252**, 289 (2001).

<sup>26</sup>V. Klymko, A. Nadtochiy, and I. Ostrovskii, *IEEE Trans. Ultrason. Ferroelectr. Freq. Control* **55**, 2726 (2008).

<sup>27</sup>I. E. Kuznetsova, B. D. Zaitsev, A. A. Teplykh, and S. G. Joshi,

- [Tech. Phys. Lett. \*\*32\*\*, 1033 \(2006\).](#)
- <sup>28</sup>T. R. Meeker and A. H. Meitzler, in *Physical Acoustics: Principles and Methods* Vol. 1, Pt. A, edited by W. P. Mason (Academic, New York, 1964) pp. 112–169.
- <sup>29</sup>I. A. Viktorov, *Rayleigh and Lamb Waves: Physical Theory and Applications* (Plenum, New York, 1967) (translation from Russian).
- <sup>30</sup>B. A. Auld, *Acoustic Fields and Waves in Solids* (Wiley, New York, 1973).
- <sup>31</sup>R. S. Wagers, in *Physical Acoustics: Principles and Methods*, edited by W. P. Mason (Academic, New York, 1977), Vol. 13, pp. 49–78.
- <sup>32</sup>S. G. Joshi and Y. Jin, *J. Appl. Phys.* **70**, 4113 (1991).
- <sup>33</sup>Yu Jin and S. G. Joshi, *IEEE Trans. Ultrason. Ferroelectr. Freq. Control* **43**, 491 (1996).
- <sup>34</sup>I. E. Kuznetsova, B. D. Zaitsev, S. G. Joshi, and I. A. Borodina, *IEEE Trans. Ultrason. Ferroelectr. Freq. Control* **48**, 322 (2001).